Flow Measurement and Instrumentation 47 (2016) 1–9

Contents lists available at ScienceDirect

Flow Measurement and Instrumentation

journal homepage: www.elsevier.com/locate/flowmeasinst

Industrial tomography using three different gamma ray

C.H. de Mesquita, A.F. Velo, D.V.S. Carvalho, J.F.T. Martins, M.M. Hamada *

Instituto de Pesquisas Energéticas e Nucleares – IPEN/CNEN-SP, Av. Prof. Lineu Prestes, 2242 São Paulo, Brazil

ARTICLE INFO

Article history:
Received 10 November 2014
Received in revised form
23 August 2015
Accepted 2 October 2015
Available online 9 October 2015

Keywords:
Computed tomography instrumentation
Detector instrumentation
Gamma-ray attenuation
Multisource tomography
Multiphase industrial process

ABSTRACT

This study describes the development of a multisource computed tomography (CT) system that proved to be a useful tool to study multiphase systems. In this CT system, two different radioisotope sources, ^{192}Ir (317 keV and 448 keV) and ^{137}Cs (662 keV), were placed in a single lead collimator and several tomography measurements carried out. The multisource CT system was capable of determining as well as differentiating the attenuation coefficients of materials with two phases (gas and liquid). It was also able to provide important information concerning the hydrodynamics occurring inside a multiphase column.

1. Introduction

Multiphase systems are structures that contain a mixture of solids, liquids and gases inside a chemical reactor or pipes in a dynamic process. These systems are widely used by the chemical, food, pharmaceutical and petrochemical industries. The gamma ray CT system has been applied to visualize the distribution of multiphase systems, providing analysts and engineers the means to obtain measurements in real time without actually interrupting production. CT systems have been used to improve design, operation and troubleshooting of industrial processes. Computer tomography for multiphase processes is now a promising technique being developed at several advanced research laboratories [1–12].

Scanners for transmission tomography employ X ray or radioisotope sources positioned on one side of the object to be scanned and one, or a set of, collimated detectors arranged on the opposite side [5–7,12–14]. Currently, scanners typified as third [1,5,11,13,15] and fourth generations [3,16] are commonly used in industrial applications. Usually, the third generation CT systems have better spatial resolution [15], while gamma ray fourth-generation scanner systems characterized as static scanners have enhanced temporal resolution (time needed to obtain an image). Also it is capable of generating images at a faster rate but generally with lower spatial resolution on dependence of its lower number of detectors. On the other hand, if spatial resolution is an important needs and knowledge of dynamic phenomena can be limited to their trends, then third generation scanner systems should be a suitable choice [16].

Usually, the analyzed objects in the industrial tomography field, such as distillation columns and engines, contain materials with a large range of densities, for example iron (7.8 g/cm^3), aluminum (2.7 g/cm^3), water (1.0 g/cm^3), gases (0.000125 g/cm^3). Thus, ideally, radioactive sources containing different gamma energies should be used. The combination of ^{137}Cs with ^{192}Ir or ^{137}Cs with ^{75}Se could be used as their energy spectra present energy peaks of 662, 468, and 317 keV for a ^{137}Cs+^{192}Ir combination or 662, ≈132, ≈269 and 401 keV for a ^{137}Cs+^{75}Se combination. Moreover, in case the object to be analyzed contains high-density material, the ^{60}Co (1173 and 1332 keV) can be included in the source combination to allow the beam to cross the materials. However, depending on the density and dimension of the object the ^{241}Am (59 keV) can be added to the source combination in order to improve the image quality in the regions where low density material is present. Moreover, if the image details of the object edge are important for the analysis, thus photons with low energy are preferable because the path of radiation absorption in the object edge is relatively small [15].

CT systems measure linear attenuation coefficients, μ (cm^{-1}) which depends on material density. Generically, high-density material implies a reduction of the transmitted beam. According to the attenuation exponential law (Beer–Lambert's law), the fraction of a beam from high-energy radiation that crosses an object of high density is higher when compared to that low-energy radiation. This effect is caused by the decrease of the mass coefficient μ (cm^{-1}) as the energy of the radiation increases (see Fig. 7). Thus,

* Corresponding author.
E-mail address: mmhamada@ipen.br (M.M. Hamada).

http://dx.doi.org/10.1016/j.flowmeasinst.2015.10.001
0955-5986/

for objects containing different density materials, ideally, the tomographic measurement should be carried out, using different energies from gamma rays. In this case, the CT data acquisition system should have the ability to discriminate between different gamma ray energies. An arrangement with ^{192}Ir ($\approx$317 and $\approx$468 keV), ^{137}Cs (662 keV) and ^{60}Co (1173 and 1332 keV) sources meets this need. Alternatively, depending on the density profile of the multiphase components, a single radioisotope source, such as ^{75}Se ($\approx$132, $\approx$269 and 401 keV), could be used [15].

In order to analyze multiphase objects, some laboratories use two radiation sources positioned at 90 degrees to each other and two sets of detectors with their respective monochannel counters [17]. However, this option has the inconvenience of needing a double set of detectors and counters. Instead, fast multichannel counters with a only set of detectors can be used. This alternative meets the requirements of the CT system for multiphase system analysis more efficiently since the number of shielded sources, detectors and counters are reduced.

In this study, a third generation multi-source transmission computed tomography system with a multichannel data acquisition electronic system was developed. Two different radioactive sources, ^{192}Ir ($\approx$317 keV yield=87%; 468 keV yield=48% and 604 keV yield=8%) and ^{137}Cs (662 keV) were placed in a single lead collimation system. The capacity of this CT system to determine and differentiate the attenuation coefficients of materials with two phases (gas and liquid) was studied using different radioisotope energies and a bubble column (ϕint=8 cm).

2. Equipment and experimental procedures

2.1. CT description and radioactive Sources

A third generation computed tomography system was developed for industrial applications at the CTR-IPEN [5,15]. In its configuration, an array of five NaI(Tl) detectors of 5×5 cm^2 (diameter, thickness) were placed on a gantry, in an arc, opposite the gamma ray sources (Fig. 1). The entire apparatus (gantry with detectors and gamma sources) rotated around the stationary object, by means of a stepper motor controlled by a host computer. The five NaI(Tl) detectors were individually collimated with lead. Each collimator had a hole of $2 \times 5 \times 50$ mm^3 (width, height, depth) for beam sampling. Two different radioactive sources, ^{192}Ir (12.2 GBq≡330 mCi) and ^{137}Cs (3.3 GBq≡89 mCi), were placed together into a radioactive source case and measured simultaneously in the tomography experiments. Fig. 2 shows the illustration of the multichannel modules device, whose electronic system (Fig. 2) contains up to 12 multichannel boards (8 bits resolution, 256 channels/board) each with its own individual high voltage (HV) supply and a circuit to control three step-motors. For this application, 256 channels/detector are enough and the ADC used presents high-speed conversion time ($\approx$800 ns/ conversion).

Considering all the circuitry (Fig. 3), the total time necessary to processing a signal is 8.4 μs per incident photon [13,14]. For each channel, the accumulated count is stored in three bytes, thus each channel has a capacity to accumulate 16,777,216 ($2^{3\times8}$) counts/channel and 4,294,967,296 counts in the 256 channels. The speed of data acquisition was the main criterion used to design the described multi-channel analyzer. The electronic circuitry and the electronic pulse profile are shown in Fig. 3. A typical ^{192}Ir and ^{137}Cs spectrum is shown in Fig. 4.

Before the tomography measurements, the five detectors were pre-adjusted using a ^{137}Cs source. The gain of each detector amplifier was adjusted in order to keep a similar spectrum profile for all detectors. After that, measurements for each detector were carried out, using two different radioactive sources (^{137}Cs and ^{192}Ir) separately. The

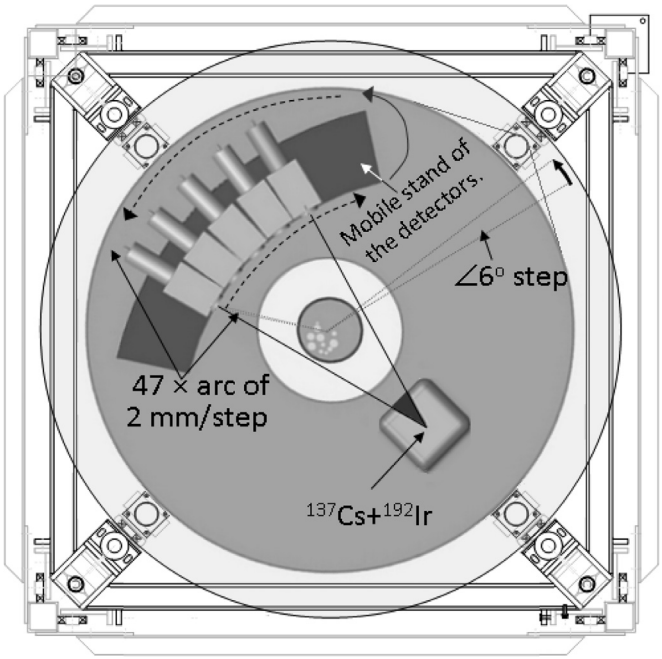

Fig. 1. Diagram of the third generation CT scanner used.

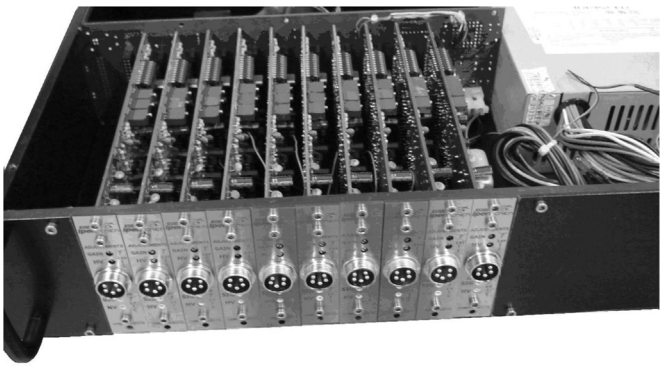

Fig. 2. The multichannel modules.

spectrometric measurements were then performed, interposing lead absorbers, between the source and the detector set. Lead absorbers from 0 to 1.5 cm thick, were sequentially interposed in order to define the degree of spectrum overlap factors. After these preliminary adjustments, the ^{192}Ir and ^{137}Cs sources were placed together in a lead shield, and the combined spectrum was measured in order to select the counting windows, as shown in Fig. 5. For all windows, the counting levels were up to 10,000 counts/10 s to assure the measurement errors below of 1% (Poisson error=square root of counts). Tomography measurements were performed by 10 s/acquisition for each one of the 2820 measurements/detector per image. For each measurement, the count sum Σ_{Cs} of the channels contained in the ^{137}Cs peak window (120–160 channels) was calculated (Fig. 5).

This value was multiplied by the factors 0.28 and 0.31 for the fractional overlap spectrum of ^{137}Cs and ^{192}Ir in the 468 keV and 317 keV windows, respectively (Fig. 5). Finally, the counts of 468 keV (Σ_{Ir468}) and 317 keV (Σ_{Ir317}) windows from ^{192}Ir were subtracted from the contribution of ^{137}Cs.

2.2. Tomography measurements

A multiphase phantom was designed and prepared to evaluate

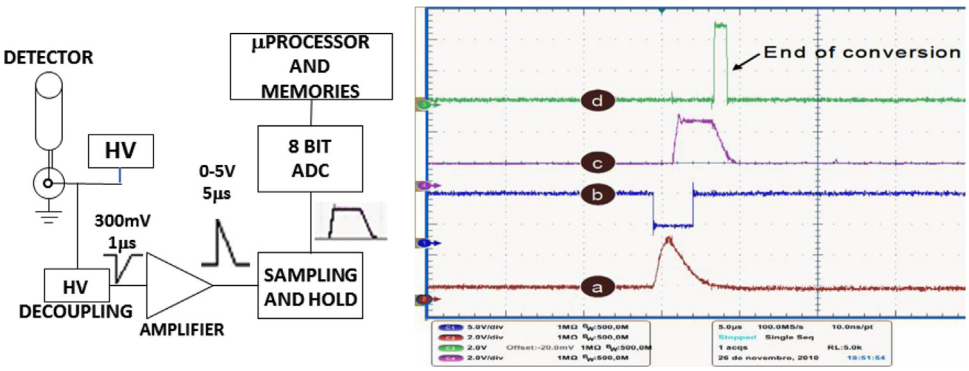

Fig. 3. Multichannel board diagram (left) and MCA (Multichannel analyzer) signal profiles (right): (a) input signal after last amplification stage, (b) triggering sampling signal, (c) after sample-and hold circuit which is the signal that will be digitized by the ADC and (d) the signal that informs the CPU that the conversion has finished (at the fall edge).

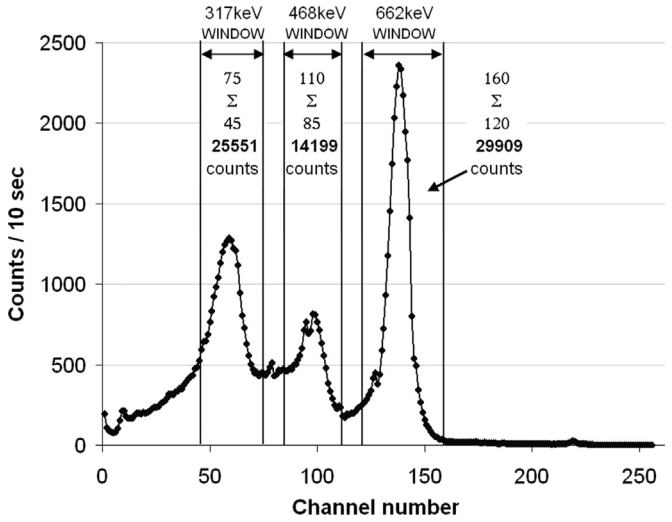

Fig. 4. A typical ^{137}Cs and ^{192}Ir combined spectrum. At the end of the acquisition time (10 s), the device (Fig. 2) integrates the sum of counts in each predefined window (selected by the user). In this data acquisition example, ^{137}Cs Σ(120–160 channels)=29,909 counts, ^{192}Ir at 468 keV Σ(85–110 channels)= 14,199 counts and ^{192}Ir at 317 keV Σ(45–75 channels)=25,551 counts.

the performance of the multisource third generation tomography device. The phantom consists of a polymethylmethacrylate (PMMA) solid cylinder (density $\delta_{PMMA}\cong 1.18$ g/cm^3) containing three holes: one filled with a steel plug ($\delta_{Fe}=7.9$ g/cm^3), another with an aluminum plug ($\delta_{Al}=2.7$ g/cm^3) and the third one with a two mm glass wall thickness ($\delta_{Glass}=2.21$ g/cm^3) tube filled with air ($\delta_{AIR}=0.001225$ g/cm^3), as illustrated in Fig. 6. In Fig. 6 below left are the dimensional data of the phantom. Right idealized images, drawn in CAD cam.

The multisource CT system was evaluated using a bubble column built with a Perspex cylindrical tube of density $\delta_{Perspex}\cong 1.2$ g/cm^3, $\varnothing_{int}=8$ cm internal diameter, $\varnothing_{ext}=9$ cm external diameter (0.5 cm wall thickness) and 140 cm height. The following parts comprised the column: liquid circuit (water), a gas circuit bubbled into a system containing a limiting hole of 0.5 cm located at 2.5 cm from the center of the column (1.5 cm from the column wall). The tomographic measurements were carried out using: (a) the column filled with water and after that (b) the column was bubbled, i.e. the water is aerated by introducing gas (5 l/ min) into the bottom, forming the bubbles. The bubbles rise to the top of the column at a speed of about 5 cm/s. For the bubble column, the tomographic measurements were taken along the column at four positions above the point of bubble generation: 5 cm, 10 cm, 20 cm and 30 cm (Fig. 8).

The CT scans were carried out for both objects separately (phantom and bubble column), by rotating the table containing the gantry with the gamma source-detector assembly, around the column through 360° in 6° stepwise intervals, generating 60 views. The movement of the detector–collimator assembly was controlled by another steeper motor; during each view this subassembly rotated 0.79°, generating 47 ray projections per detector or 235 (47 steps × 5 detectors) ray projections per view totaling 14,100 (235 × 60) ray projections per image. The estimate time waste to generate a tomographic image is around 8hours (14,100 ray projections × 10 s/5 detectors/ 3600 s/h).

All five detectors had a diameter of 50 mm surrounded by 50 mm thick lead. Thus, the distance between the centers of one detector to another was ≈150 mm (25+25+50+50 mm). The radiation reaches the detector through 2 × 5 mm rectangular hole. To increase the spatial resolution, the detectors must move 50 times through a 2 mm step arc. Thus, the gantry system, shown in Fig. 1, operates as an emulator of a position sensitive detector. In this third generation tomography, the spatial resolution was privileged against the temporal resolution. The used CT scanner has a

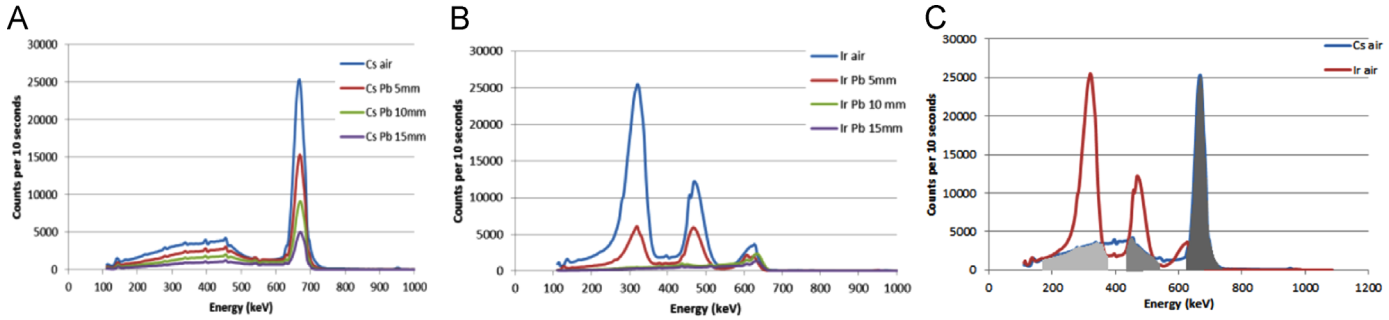

Fig. 5. ^{137}Cs (A) and ^{192}Ir (B) spectra at different attenuation levels. The ^{137}Cs overlaps the ^{192}Ir spectrum (C). The experimental sources used for the overlapping factors of the spectra were: 0.28 ± 0.13 at 468 keV and 0.31 ± 0.19 at 317 keV.

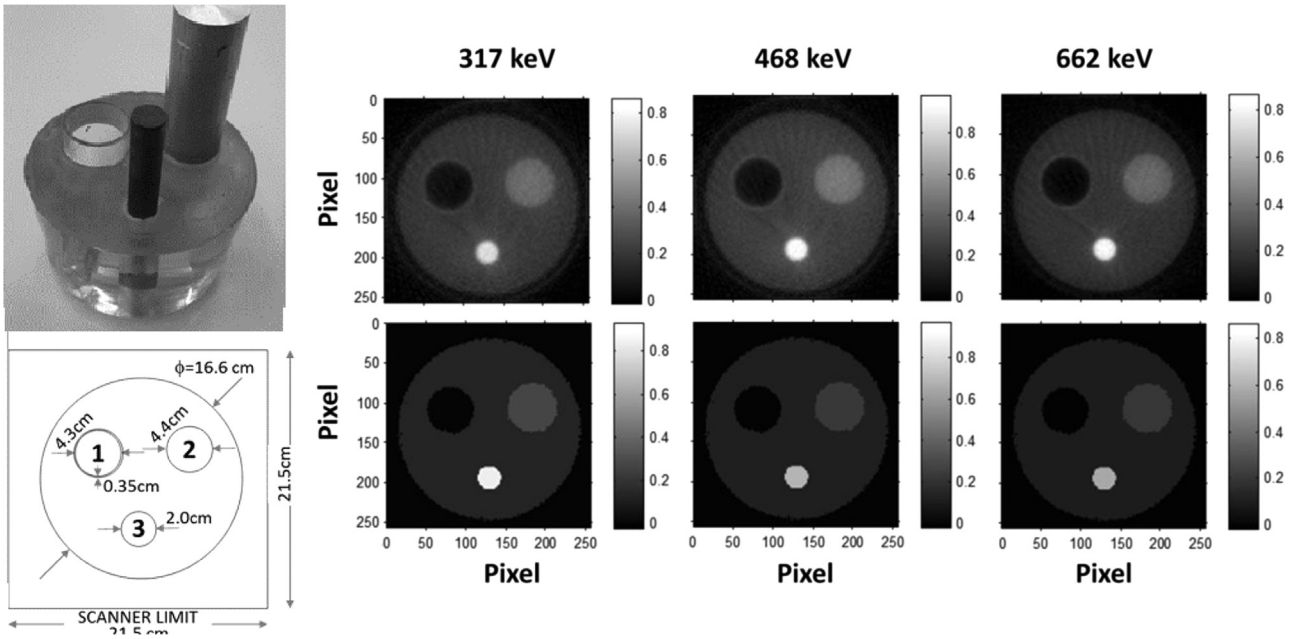

Fig. 6. Reconstructed images from sampled tomograms at different radiation energies. Reconstructed images (top) and idealized images (bottom).

spatial resolution range of 0.48–49.5 cm, depending on the radioactive source energy and the material density. For 10-second acquisition measurements, the temporal resolution is about 8hours/image.

2.3. The image reconstruction and statistical analysis

For comparisons, images were reconstructed with a resolution of 256×256 pixels for each photon energy level: 317 keV, 468 keV and 662 keV, using the SMART (String Matching Algorithms Research Tool) algorithm [18]. In the reconstructed images, the phantom shows a diameter of ≈ 200 linear pixels for its actual value of 166 mm (Fig. 6). Thus, each pixel is equivalent to 0.83 mm (⌀166 mm/↔200 linear pixel) and a estimated voxel of 3.4 mm^3 ($(0.83\ mm)^2 \times 5$ mm collimator height). The results were compared, evaluating the reconstructed images qualitatively (visually) and quantitatively by the analysis of the following statistical parameters: the median $\tilde{\mu}$ (cm^{-1}), the lower $\tilde{\mu}_{q1}$ (cm^{-1}) and upper $\tilde{\mu}_{q3}$ (cm^{-1}) quartiles, the mean $\bar{\mu}$ (cm^{-1}) and the RMSE (Root-mean-square deviation) of the data set $\mu_{i,j}$ (cm^{-1}), the attenuation coefficient calculated for the pixel at the (i,j)-th position from the reconstructed image.

The arithmetic mean was defined as:

$$\bar{\mu} = \frac{\sum_{i=1}^{N_1} \sum_{j=1}^{N_2} \mu_{i,j}}{N_1 \times N_2} \quad (1)$$

The number $N_1 \times N_2$ of pixels in the material region depends on the area that surrounds each material inside the phantom, as shown in Fig. 6. Particularly, $N_1 \times N_2 = (29 \times 29) = 1841$ pixels in the inscribed square area for the air, acrylic and aluminum and $N_1 \times N_2 = (25 \times 25) = 625$ pixels for the steel area. These areas were arbitrarily selected taking in account the diameters of the objects inside the phantom.

The figure of merit RMSE was calculated according to equation (2):

$$\mathrm{RMSE} = \sqrt{\frac{\sum_{i=1}^{N_1} \sum_{j=1}^{N_2} (\mu_{i,j} - \hat{\mu}_{i,j})^2}{N_1 \times N_1}} \quad (2)$$

where, $\bar{\mu}_{i,j}$ (cm^{-1}) is the respective attenuation value from the idealized figure shown in the bottom-right of Fig. 6, which was created in CAD software.

The statistic parameters: mean $\bar{\mu}$ (cm^{-1}), median $\tilde{\mu}$ (cm^{-1}) and quartiles $\tilde{\mu}_{q1}$ (cm^{-1}) and $\tilde{\mu}_{q3}$ (cm^{-1}) were calculated by the SigmaStat for Windows version 3.5 (Systat Software, Inc.; Point Richmond, CA-USA).

The statistical significance of the radiation energies, on the image quality, was evaluated by the Friedman Repeated Measures Analysis of Variance on Ranks. The comparisons among groups and the statistical parameters were calculated with the SigmaStat software. For quantitative analysis, the following parameters were considered: the median $\tilde{\mu}$ (cm^{-1}); the difference between quartiles ($\Delta\tilde{\mu}_{q_{3-1}} = \tilde{\mu}_{q_3} - \tilde{\mu}_{q_1}$); the mean $\bar{\mu}$ (cm^{-1}) and the RMSE. Among groups (air, acrylic, aluminum and steel), the lowest value of each parameter was used to define the best-reconstructed image quality.

3. Results and discussion

The energy spectra of ^{192}Ir and ^{137}Cs (Fig. 5) were obtained from attenuation with lead sheets in thicknesses of 0.5 cm, 1.0 cm and 1.5 cm. The pulse height spectra are attenuated as the absorber thickness increases (Fig. 5(A) and (B)). The Compton scatter region for ^{137}Cs overlaps the ^{192}Ir photopeaks, which are almost constant, regardless of the absorber thickness. In the present case, the ^{137}Cs superimposed the ^{192}Ir region of 468 keV by a factor of 0.28 ± 0.13 and the 317 keV regions by a factor of 0.31 ± 0.19, (Fig. 5 C)

In the image reconstruction, the logarithm of the ratio I_0/I was used. In practical terms, the ^{137}Cs values of I_{0Cs} and I_{Cs} do not need overlay corrections because the contribution from the ^{192}Ir in the ^{137}Cs peak region counting is almost nil. The same, however, is not valid for both peaks of the ^{192}Ir source. In this case, the corrections were:

$$\hat{I}_{0Ir468} = I_{0Ir468} - 0.28 \times I_{0Cs} \quad (3)$$

$$\hat{I}_{Ir468} = I_{Ir468} - 0.28 \times I_{Cs} \quad (4)$$

$$\hat{I}_{0Ir317} = I_{0Ir317} - 0.31 \times I_{0Cs} \quad (5)$$

$$\hat{I}_{Ir317} = I_{Ir317} - 0.31 \times I_{Cs} \quad (6)$$

where, $\hat{I}_{0Ir468}$ and $\hat{I}_{0Ir317}$ are the corrected values concerning the measurements without the object in front of the ^{192}Ir source for photopeak windows of 468 keV and 317 keV, respectively. $\hat{I}_{Ir468}$ and $\hat{I}_{Ir317}$ are the corrected values for measurements of 468 keV and 317 keV, respectively, when the object (the column) is in front of the ^{192}Ir beam source. Finally, I_{Cs} is the corresponding photopeak window counting of ^{137}Cs source.

One may ask, is it really necessary to correct the overlap peaks? Conceptually, the histogram is derived from the calculation of $\log_e(I_0/I)$, where I_0 for each detector is a constant $\pm$ the Poisson fluctuation ($\pm$ the square root of the constant I_0). The same applies to $\hat{I}_{0Ir468}$ (Eq. (3)) and $\hat{I}_{0Ir317}$ (Eq. (5)) since all terms on the right side of the equations are constants (or near constants). However, the same does not apply for $\hat{I}_{Ir468}$ and $\hat{I}_{Ir317}$ in Eqs. (4) and (6) because, according to attenuation exponential law, their values are not constant and they will depend on the absorption of the beam during their paths in the NaI(Tl) detector. On the other hand, the Compton generated in the object is not significant due to lead collimator protection effect in the detector.

3.1. Analysis of the phantom images

The reconstructed images for each of the three photon energies: 317 keV, 468 keV and 662 keV using the multiphase phantom are shown in Fig. 6. Images were reconstructed with the SMART algorithm.

3.2. Qualitative analysis

In visual terms, the figure generated with 317 keV seems to present the best image, mainly in the area of the air content. In the contour of this region, the thin glass material (3.5 mm wall thickness) can be observed in Fig. 6. This glass was bonded permanently to the plastic matrix during its polymerization for building the phantom. In addition, in the aluminum region, the 317 keV image seems to be more intense and the $\varnothing$=2 cm steel region is well delineated. Similar observations can be seen for 468 keV, although with less emphasis. Finally, the image for 662 keV suggests a better circular contour for the $\varnothing$=4 cm aluminum material and a better color uniformity for the $\varnothing$=2 cm steel material.

The parameter MTF (Modular Transfer Frequency) is a manner to express the image resolution. Fig. 7 shows the MTF analysis for the present study. According to Fig. 7 the scanner with 317 keV shows mathematically better results for the materials containing in the phantom used.

3.3. Quantitative analysis

The images shown in Fig. 6, each (i,j)th-pixel color represents a numeric value which is the mass attenuation coefficient $\mu_{i,j}$ (cm^{-1}) for the material contained in the respective object pixel (or voxel). For an ideal tomographic image, pixels contained same material should same value of $\mu_{i,j}$ (cm^{-1}). In other words, the $\mu_{i,j}$ (cm^{-1}) is a function of the material density and the incident γ-radiation energy. However, in practice, for same material, $\mu_{i,j}$ (cm^{-1}) is not a constant but rather subject to relative random variation which depends on the experimental conditions. The

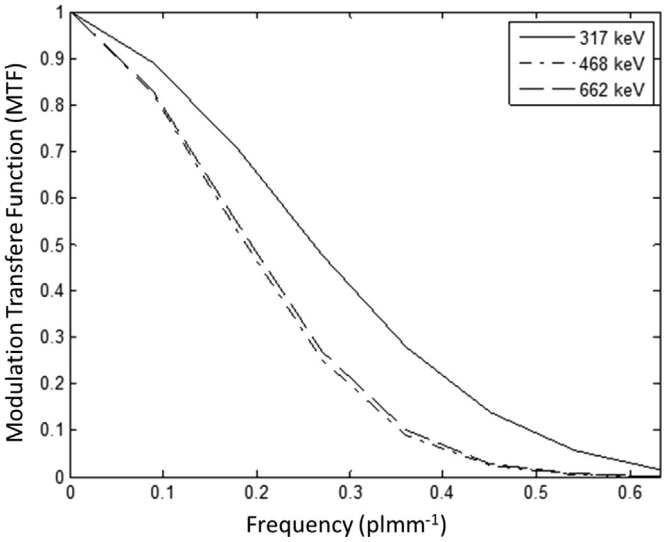

Fig. 7. Modulation Transfer Function.

statistic theory is a suitable tool to compare data set, which varies randomly. The statistical tests were used to verify if two or more groups were significantly different. Basically, there are two types of numeric data: (1) those data whose variation fit the normal distribution (a Gaussian function) and (2) those data that do not obey the Normal distribution. The first task of an analyst is to recognize to which distribution type this data belongs to. For this purpose, the Kolmogorov–Smirnov Normality Test [19] can be used. After that, the analyst must choose the statistical test for applying the comparisons. To compare multiple groups simultaneously, the Tukey test is one of the most suitable.

In the present paper the Normality Test (Kolmogorov–Smirnov) indicated that for all $\mu_{i,j}$ groups (air, aluminum, iron and acrylic) when used 317, 468 and 662 keV do not meet the normality distribution criterion at $P < 0.001$. This fact indicates that the $\mu_{i,j}$ dataset (the selected area surrounding each object) vary, significantly, from the pattern expected if the $\mu_{i,j}$ data were drawn from a population with a normal distribution. This finding can be easily explained. Within the boundaries of each region, there are actually two populations. For example, in aluminum sample region (a rectangle of 29×29 pixels) is constituted by two population densities: (a) aluminum and (b) acrylic. The same applies to the other regions studied. Consequently, the lack of normal distribution implies the use of the mean together with its standard deviation, which is not suitable to characterize the $\mu_{i,j}$ dataset. In this case, the median $\tilde{\mu}$ and the first $\tilde{\mu}_{q_1}$ and third $\tilde{\mu}_{q_3}$ percentiles are more suitable to define the experimental (the index color of reconstructed image) distribution of the $\mu_{i,j}$ dataset population. Another experimental finding was that all statistical comparisons were shown to be significantly different at $P < 0.05$ for all groups studied (Table 1).

The values of the parameters shown in the Table 1 were used to quantify the images. The smaller the $\tilde{\mu}$ median value, the better is the image quality. The same is valid for all other parameters: (a) the difference between the percentiles $\Delta\tilde{\mu}_{q_{3-1}} = \tilde{\mu}_{q_3} - \tilde{\mu}_{q_1}$ and (b) the arithmetic means $\bar{\mu}$ and (c) the RMSE.

Classically, in the tomography field, the RMSE parameter defined by Eq. (2) is the most common parameter used for image quality evaluation [20] is the standard deviation of the distribution (Eq. (2)), thus the RMSE should be used with caution to qualify the image quality.

The parameters used to endorse the quantitative analysis are summarized in Table 1.

For low-density material such as gases, smaller values were

Table 1
Statistical analysis of the image parameters, Median and its confidence interval: RMSE figure of merit and the comparative analysis for materials of different densities scanned with different energies. For each group the best results are shaded.

Material	Number of pixels in region	Energy (keV)	Median $\tilde{\mu}$ (cm^{-1})	Percentiles			Mean $\bar{\mu}$ (cm^{-1})	RMSE (cm^{-1})	Comparison	$P<0.05$
				$\tilde{\mu}_{q1}$ (cm^{-1})	$\tilde{\mu}_{q3}$ (cm^{-1})	$\Delta q_{3-1}\tilde{\mu}_{q3}-\tilde{\mu}_{q1}$ (cm^{-1})				
Air	841	317	0.000149	0.000149	0.0447	0.0446	0.0234	0.0404	468 vs 317	Yes
		468	0.000124	0.000124	0.0691	0.0690	0.0325	0.0524	468 vs 662	Yes
		662	0.000103	0.000103	0.049	0.0489	0.0237	0.0395	662 vs 317	Yes
Acrylic	841	317	0.139	0.116	0.162	0.0460	0.140	0.165	468 vs 317	Yes
		468	0.117	0.109	0.127	0.0180	0.118	0.133	468 vs 662	Yes
		662	0.101	0.098	0.106	0.0085	0.103	0.082	662 vs 317	Yes
Aluminum	841	317	0.272	0.219	0.348	0.1290	0.295	0.110	468 vs 317	Yes
		468	0.240	0.166	0.365	0.1990	0.285	0.163	468 vs 662	Yes
		662	0.205	0.152	0.283	0.1310	0.231	0.108	662 vs 317	Yes
Steel	625	317	0.842	0.418	0.842	0.4240	0.646	0.307	468 vs 317	Yes
		468	0.701	0.329	0.701	0.3720	0.530	0.268	468 vs 662	Yes
		662	0.580	0.316	0.581	0.2650	0.451	0.205	662 vs 317	Yes

obtained for $\Delta q_{3-1}=0.0446$, and the mean $\bar{\mu}=0.0234$, therefore, suggesting that 317 keV was the best energy for scanning gas materials. However, the median $\tilde{\mu}=0.000103\ cm^{-1}$ and the RMSE=0.0395 indicate that the 662 keV is the better photon energy. These results are ambiguous and as such do not allow us to reach a clear conclusion. For gaseous materials both energies (317 or 662 keV) were capable of generating tomographic images of similar quality, although the qualitative analysis, described above and based on Fig. 8, suggests that the energy of 317 keV was better for scanning gaseous materials.

For acrylic material, all parameters (median $\tilde{\mu}$, difference of percentiles Δq_{3-1}, mean $\bar{\mu}$ and RMSE) presented the best results for the scans carried out with 662 keV, which are the smallest values. For aluminum, most parameters showed better results for 662 keV, the exception being for the percentile difference $\Delta\tilde{\mu}_{q_{3-1}}=0.1290\ cm^{-1}$ which showed 317 keV as the smallest value.

The worse results were obtained for 468 keV (Table 1). However, this cannot be considered as a global assertion, because the poor performance found may be caused by the low net activity of the 468 keV peak, compared to other energies, as can be observed in Figs. 4 and 5. This effect was already considered in the section II-B (Qualitative Analysis) concerning to theory for the best possible counting statistics (minimum counting error) [20].

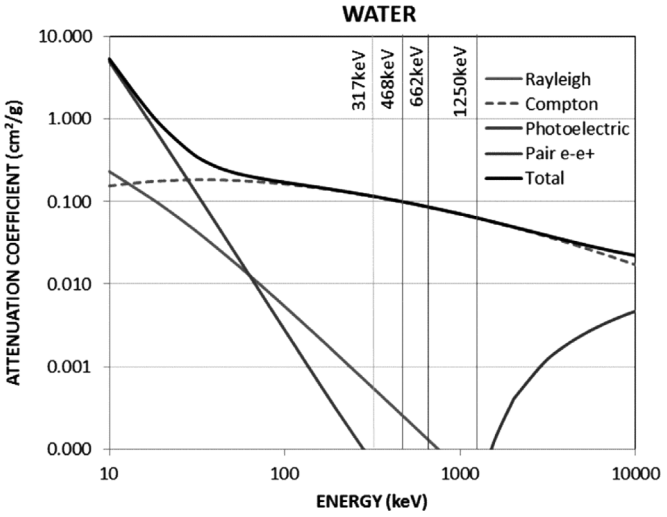

Fig. 8. Main processes of radiation interactions with water and their mass attenuation coefficients as a function of photon energy. The solid black line represents the total attenuation coefficient. Compton scattering is the major contribution among others interactions type. Data from NIST National Institute of Standards and Technology.

Considering qualitative and quantitative analyses, it may be concluded that it is advantageous to use multisource to scan industrial objects containing several materials, with large density differences. It should be emphasized that, for quantitative analysis, other parameters should be applied in addition to classical RMSE. As can be seen in Table 1, if only RMSE parameters had been applied, the scans at 662 keV would have been selected as being the best. However, the other two parameters (Δq_{3-1} and mean $\bar{\mu}$), in association with qualitative analysis, suggest 317 keV as the best energy for scanning gases.

According to Fig. 8, data extracted from NIST [21], the range of energies used (317 to 662 keV) presented small attenuation coefficient differences, ranging from 0.118 cm^2/g for 317 keV to 0.086 cm^2/g for 662 keV, with a variation of only 27% between them. In this type of experiment, better results could be obtained, by expanding the photon energy range, for example, using radioactive sources with photon energies of 60 keV ^{241}Am and ~1250 keV ^{60}Co. However, the decision to expand the energy range may conflict with experimental constraints. For example, if a distillation column is made up of a very dense material, the 60-keV radiation may be completely absorbed in the wall of the object and it will not contribute to the tomographic imaging.

Ideally to achieve a good energy-range choice, the mass attenuation coefficients should be as widely separated as it can be possible.

In short, in agreement with the qualitative analysis, the 317 keV and 662 keV images resulted in a better image quality for most of the items considered. The image from 468 keV could have presented similar quality, but the low net activity at 468 keV produced an image noisier outcome, compromising the tomography performance. On the other hand, for relative dense materials such as aluminum and steel, the 662 keV images showed better edge definition. For lower density materials such as air, the 317 keV presented better performance.

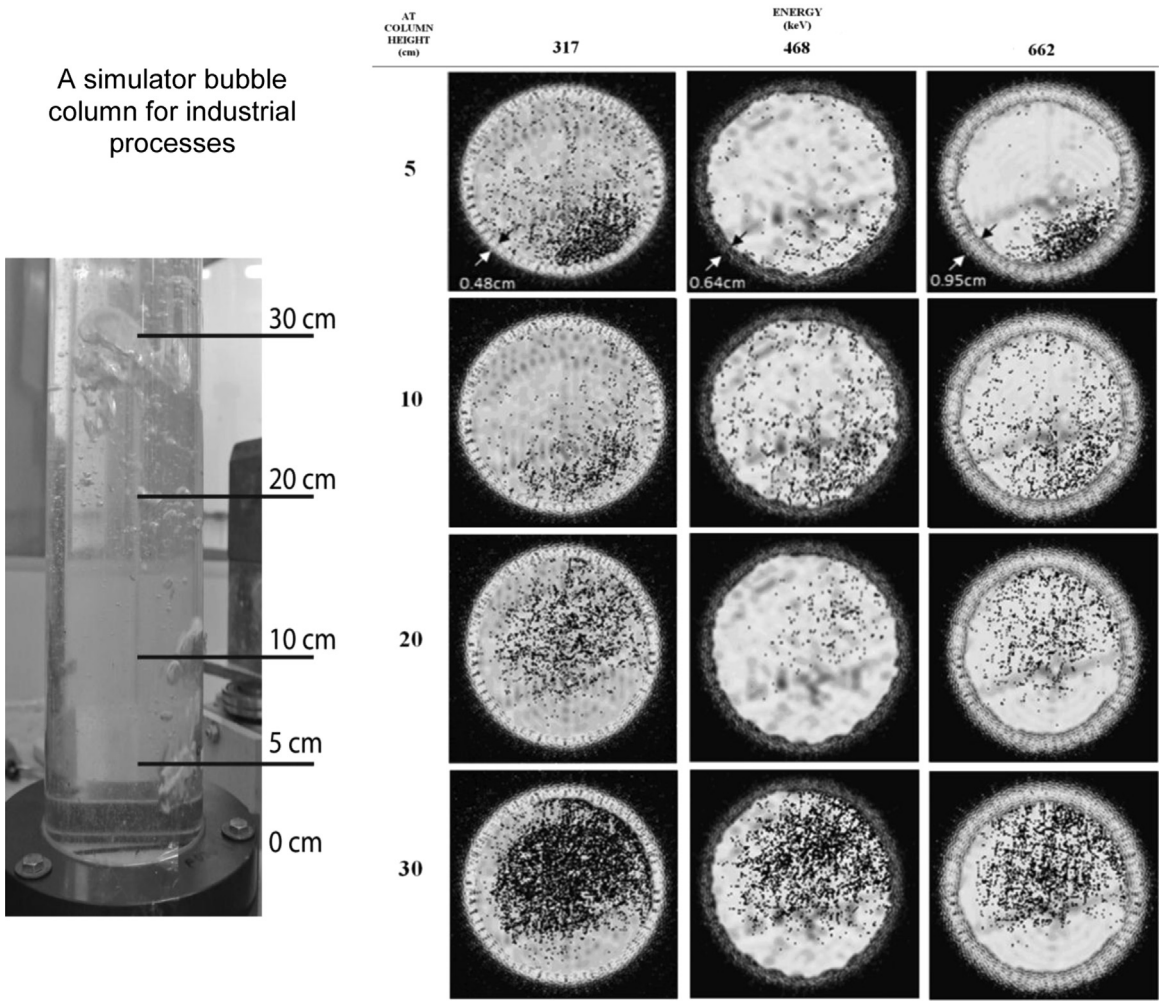

Fig. 9. Reconstructed images performed for different energies, at four distances from the bubbles generation center. For the reconstruction images relative to 5 cm height distance, the estimate determined for the polymethylmethacrylate (PMMA) column thickness, '*d*', is showed in the "→ *d* ←" label for three energies.

3.4. Analysis of the bubble column

The picture of the acrylic column ($\delta \cong 1.2$ g/cm^3), filled with water ($\delta = 1.0$ g/cm^3) and air ($\delta = 1.25 \times 10^{-3}$ g/cm^3) bubbled at 5 l/min prepared to simulate the bubble columns is showed in Fig. 9. As it can be observed in this figure, the bubble-generating center is close to the column wall and the bubbles undergo a spreading process along the column with a tendency to move to the opposite side wall as they rise along the column. The bubbles originate with a relatively large size and during their rise along the column they subdivide into smaller bubbles. The image reconstructed from the tomography measurement data should reproduce this morphology. As it can be observed in the Fig. 9, all images satisfy this expectation.

The column wall thicknesses were 4.8, 6.4 and 9.5 mm for 317, 468 and 662 keV, respectively; according to the image from Fig. 9. The actual size is 5 mm. When a standard phantom is not available to calibrate the CT system, the spatial resolution may be estimated as the size difference between the experimental value and the actual size of the object. Thus, the spatial resolutions were 0.2 mm (5.0–4.8 mm) for tomographic acquisition with 317 keV, 1.4 mm (6.4–5 mm) for 468 keV and 4.5 mm (9.5–5 mm) for 662 keV. These results confirm that lower energies are capable of generating images with higher spatial resolution, for small materials with density in the order of 1 g/cm^3, like water and acrylic. On the other hand, high energy, here represented by ^{137}Cs radiation, showed the worse spatial resolution for small material with density close to 1 g/cm^3.

The bubbles are generated in the bottom of the column, near the wall (Fig. 9). At 30 cm above, bubbles spread out and migrate to the opposite wall with an average speed of 5 cm/s. During the ascent the bubbles, expand in volume and explode forming new small bubbles, thus increasing their numbers (Fig. 9). The used CT system is not useful for tracing or scanning individual bubbles due to its poor temporal resolution (≈ 8 h/image versus bubble speed of 5 cm/s). Thus, the images obtained in four different column positions (5, 10, 20 and 30 cm height) represent only the effect of average attenuation coefficient μ (cm^{-1}) at the (i,j)-th pixel. The small dark dots are not the bubbles but rather failures of the density in the medium due to the bubble distribution.

In the tomographic image the color index of the (i,j)-th pixel represents the weighted average attenuation coefficients for all materials contained in the respective pixel and it is weight by the concentration fraction "$\boldsymbol{c_k}$" of the k-th material (phase) in the pixel region, or mathematically speaking:

$$\mu_{ij}(cm^{-1}) = \frac{\sum_{k=1}^{N} (c_k \times \mu_{ij}^{k}(cm^{-1}))}{\sum_{k=1}^{N} c_k} \tag{7}$$

Table 2
Mass attenuation coefficients μ (cm^2/g) for water and air for different energies.

Material	Density δ (g/cm^3)	Mass attenuation μ(cm^2/g)[a]		
		317 keV	468 keV	662 keV
Water	1.00	0.1156	0.0993	0.0856
Air[b]	1.2×10^{-3}	0.1040	0.0893	0.0770
Ratio	833	1.1115	1.1122	1.1119

[a] From: NIST – National Institute of Standard and Technology (XCOM http://physics.nist.gov/cgi-bin/Xcom/xcom2).
[b] 78.084% N_2, 20.946% O_2 and 0. 934% Ar.

$$\sum_{k=1}^{N} c_k = 1 \tag{8}$$

where $\mu_{i,j}^{k}$ is the mass attenuation coefficient of the k-th material and N is the number of pixel in the material region.

In present study, all materials (water and air) and their densities and attenuation coefficients $\mu(cm^2/g)$ are well known and shown in Table 2. As can be inferred from the Table 2, although water is 833 times heavier than air, this difference reflects only 11% in the ratio of the mass attenuation coefficients for different energies when it is expressed as a cm^2/g unit.

The Eq. (9) converts μ (cm^2/g) to μ (cm^{-1}).

$$\mu(cm^{-1}) = \mu\left((cm^2/g) \times \delta(g/cm^3)\right) \tag{9}$$

Rewritten Table 2, in terms of μ (cm^{-1}), we obtain values shown in Table 3.

According to the attenuation exponential law $I=100e^{-\mu \cdot x}$), for $X=1$ cm thickness of water, the transparencies of the photons are 89.1%, 90.5% and 98.1% for 317, 468 and 662 keV, respectively. In this range, the maximal attenuation difference is 2.7% (98.1–89.1%). While for a 10 cm thickness of water, in the same manner, the transparencies are: 31.5%, 37.0% and 42.5%. In this case, the maximal difference is 11% (42.5–31.5%). Thus, the photon attenuation is even greater as material thickness is increased and the attenuation difference among the photon energies is also increased as expected by the law of exponential attenuation. Theoretically, the same applies to air, although with much less effect. Air is virtually transparent to radiation from 317 keV to 662 keV for small air thicknesses.

The fractional concentration $\boldsymbol{c_k}$ also called holdup [1,4,14] is useful when we are interested to discover the proportion of the materials within a distillation column (or a multiphase system) and the concentration gradients inside the object. In the present paper, the column contains, only, water and gas. To calculate their relative proportions $\boldsymbol{c}_W$ and $\boldsymbol{c}_A$ (for water and air, respectively) in a pixel at the (i,j)-th position we need to solve the matrix system of the Eq. (10), which is derived from Eqs. (7) and (8).

$$\begin{bmatrix} c_{i,j}^{W} \\ c_{i,j}^{A} \end{bmatrix} = \begin{bmatrix} \mu_W^E & \mu_A^E \\ 1 & 1 \end{bmatrix}^{-1} \cdot \begin{bmatrix} \mu_{i,j}^E \\ 1 \end{bmatrix} \tag{10}$$

Table 3
Mass attenuation coefficients μ (cm^{-1}) for water and air for different energies.

Material	Density δ (g/cm^3)	Mass Attenuation μ (cm^{-1})		
		317 keV	468 keV	662 keV
Water	1.00	0.1156	0.09932	0.08562
Air	1.25×10^{-3}	0.000125	0.000107	0.000092
Ratio	833	926.3	926.8	926.6

where μ_W^E and μ_A^E are the mass attenuation coefficients for water and air for a specific energy $\boldsymbol{E}$. In this study, both values μ_W^E and μ_A^E can be taken from Table 3. $\mu_{i,j}^E$ is the experimental mass attenuation coefficient obtained from the reconstruction image (Fig. 9) at the (i,j)-th pixel.

Fig. 10 illustrates three possibilities to understand multiphase phenomena that occur in the experimental column. While the first (Fig. 10 (A)) is easier to obtain. However, in practice it is almost impossible in an industrial environment because columns are generally opaque and its interior is rough and inaccessible. The other two possibilities are non-invasive contributions of the tomography technology. The holdup of water and air for each position of a column planar section (i.e., $\varnothing_{int}$=8 cm, 5 cm height), which was calculated for each pixel using the Eq. (10), is shown in Fig. 10 (C).

Gas holdup is shown in the bottom surface of the Fig. 10 (C) while liquid holdup can be observed at the upper. Gas holdup at 5 cm height presents a protuberance above the center of the bubble formation. In this region, the maximal value is around 0.18, which means that this region contains 18% of air and 82% of water (upper surface). Besides, the protuberance region indicated by an arrow in Fig. 10 (C), we can also observe the bubble distribution with less intensity around the column wall and in its center. In addition, the gas holdup shows a valley between the wall and center of the column. These findings agree to that observed in the tomography image (Fig. 10 (B)). The holdup analysis is an important complement to understand multiphase systems, perhaps even more useful than the image itself.

For a single energy tomography, the determination of the number N of $\boldsymbol{c_k}$ in Eq. (10) is limited to N=2, because there are only two equations in the matrix system as shown in Eqs. (7), (8) and (10). For each new k-th compound or phase inside the column, the new $\boldsymbol{c}_k$ can be determined using new photon radiation (multisource tomography technology proposed in this paper). Thus, for a column contained N > 2 phases the Eq. (10) can be rewritten as the Eq. (11): Thus this equation is a crucial argument to reinforce the thesis of the advantages of the multisource tomography technology, beyond the ability to enhance image details, considering that multiphase systems commonly have three or more phases.

$$\begin{bmatrix} c_{i,j}^{1} \\ c_{i,j}^{2} \\ \cdots \\ c_{i,j}^{N} \end{bmatrix} = \begin{bmatrix} \mu_{Phase1}^{E1} & \mu_{Phase2}^{E1} & \cdots & \mu_{PhaseN}^{E1} \\ \mu_{Phase1}^{E2} & \mu_{Phase2}^{E2} & \cdots & \mu_{PhaseN}^{E2} \\ \cdots & \cdots & \cdots & \cdots \\ 1 & 1 & 1 & 1 \end{bmatrix}^{-1} \times \begin{bmatrix} \mu_{i,j}^{E1} \\ \mu_{i,j}^{E2} \\ \cdots \\ 1 \end{bmatrix} \tag{11}$$

There is no indication that a particular energy is able to generate the best image for all regions of an object. It is more likely that each region of the object, depending on its local density, is better interpreted with a particular energy. Thus, the advantage of using the system from multiple sources is justified since the user can analyze parts of the object from different origin images. The same is true for the analysis of the holdup.

Another potential application for multisource tomography technology using the multichannel analyzers as data acquisition is the emission tomography in which radioactive tracers are introduced inside the object (for example a distillation column). In addition, multisource tomography technology can be used in other tomography generation types, such as, the fourth generation, which has fast temporal resolution. In this case, the images can be obtained very quickly, in seconds or a fraction of a second [3].

4. Conclusion

The use of a fast electronic multichannel analyzer capable to

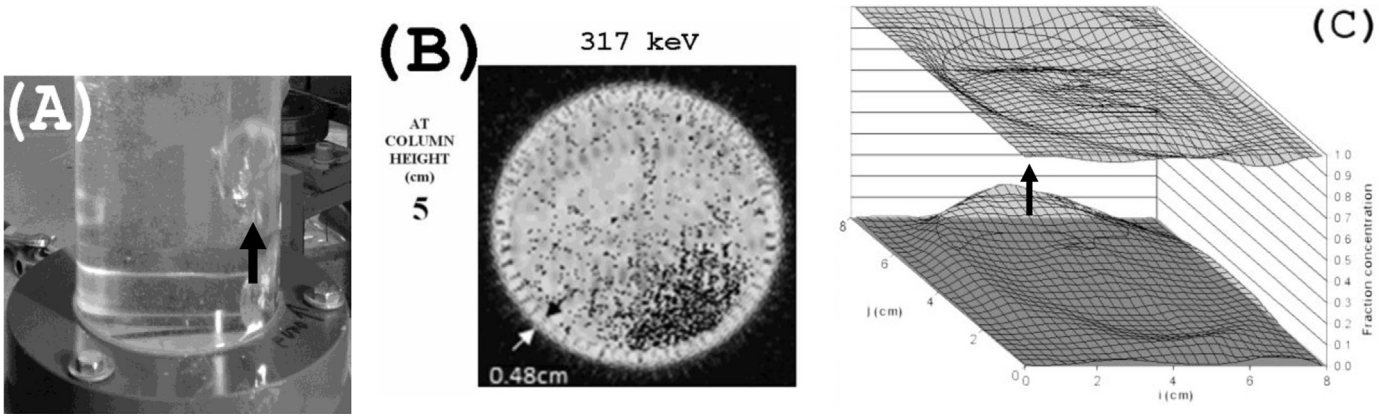

Fig. 10. For each (i,j)-th pixel from the reconstruction image (B) the c_W and c_A were calculated solving the Eq. (11) matrix system. Concentration gradients of water and air (C) in column at five cm above bubble generation (A). The arrow indicates a bubble generator position in the column bottom at 1.5 cm from the column wall.

processing a signal in 8.4 μs per incident photon proved to be adequate for the tomography of multiphase processes. This system was capable of acquiring different tomographic data with different energies, thus allowing the user to choose the counting window, which results better image quality. For multiphase column images, the object edge spatial resolutions were of 0.2 mm for tomographic acquisition with 317 keV, 1.4 mm for 468 keV and 4.5 mm for 662 keV. Industrial CT scanners with multichannel analyzers are capable of producing paired images derived from different radiation energies. For each image region, depending on the energy, the multisource system is capable of classifying the scanned object material with better performance. Preferentially, photon energy peaks should be adequately spaced so that their mass attenuation coefficient ($\mu(\mathrm{cm}^2/\mathrm{g})$) ensure statistical significance of attenuation in the objects studied. The spectral peaks should have appropriate heights so that peaks of higher energy and activities do not eclipse the peaks of lower activities. In the analysis of tomographic images it is always advisable to perform qualitative (visual) and quantitative (parametric) analysis because they are complementary. The quantitative analysis protocol should include the following parameters: median $\tilde{\mu}$, percentile difference $\Delta q_{3-1}=(\tilde{\mu}_{q_3}-\tilde{\mu}_{q_1})$, the arithmetic mean $\bar{\mu}$ and the RMSE. Thereafter, for each image region, the energy that presents the lowest values of the parameter set is selected as the best image. The holdup analysis is a potential tool to complement the image analyses.

Acknowledgments

The authors would like to express their gratitude to CNPq (Grant number 305210/2013-0) (The Brazilian National Research Council) and FAPESP (Foundation for Research Support of the State of São Paulo) (Grant number 2012/22705-3) for financial support and fellowship.

References

[1] A. Kemoun, B.C. Ong, P. Gupta, M.H. Al-Dahhan, M.P. Dudukovic, Gas holdup in bubble columns at elevated pressure via computed tomography, Int. J. Multiphase Flow 27 (2001) 929–946.
[2] A. Youssef, M.H. Al-Dahhan, Impact of internals on the gas holdup and bubble properties of a bubble column, Ind. Eng. Chem. Res. 48 (17) (2009) 8007–8013.
[3] G.A. Johansen, U. Hampel, B.T. Hjertaker, Flow imaging by high speed transmission tomography, Appl. Radiat. Isot. 4–5 (68) (2010) 518–524.
[4] L.N. Kong, W. LI, L.C. Han, Y.J. Liu, H. Luo, M.H. AL-Dahhan, On the measurement of gas holdup distribution near the region of impeller in a gas–liquid stirred Rushton tank by means of γ-CT, Chem. Eng. J. 188 (2012) 191–198.
[5] C.H. Mesquita, D.V.S. Carvalho, R. Kirita, P.A.V. Salvador, M.M. Hamada. Gas–liquid distribution in a bubble column using industrial gamma-ray computed tomography, Radiat. Phys. Chem. 95 (2014) 396–400.
[6] U. Hampel, A. Bieberle, D. Hoppe, J. Kronenberg, E. Schleicher, T. Sühnel, F. Zimmermann, C. Zippe, High resolution gamma ray tomography scanner for flow measurement and non-destructive testing applications, Rev. Sci. Instrum. 78 (1–9) (2007) 103704.
[7] A. Bieberle, H. Nehring, R. Berger, M. Arlit, H.-U. Härting, M. Schubert, U. Hampel, Compact high-resolution gamma-ray computed tomography system for multiphase flow studies, Rev. Sci. Instrum. 84 (1–10) (2013) 033106.
[8] U. Hampel, Y. Bärtling, D. Hoppe, N. Kuksanov, S. Fadeev, R. Salimov, Feasibility study for mega-electron-volt electron beam tomography, Rev. Sci. Instrum. 83 (1–7) (2012) 093707.
[9] S. Rabha, M. Schubert, F. Grugel, M. Banowski, U. Hampel, Visualization and quantitative analysis of dispersive mixing by a helicalstatic mixer in upward co-current gas–liquid flow, Chem. Eng. J. 262 (2015) 527–540.
[10] A. Bieberle, J. Kronenberg, E. Schleicher, U. Hampel, Design of a high resolution gamma-ray detector module for tomography applications, Nucl. Instrum. Methods Phys. Res. A (2007) 668–675.
[11] J. Kim, S. Jung, J. Moon, J.G. Guen Park, J. Jin, G. Cho, Development of transportable gamma-ray tomographic system for industrial application, Appl. Radiat. Isot. (2014) 203–208693 (2014) 203–208.
[12] R.E. Vieira, N.R. Kesana, B.S. McLaury, S.A. Shirazi, C.F. Torres, E. Scheicher, U. Hampe, Experimental investigation of the effect of 90 standard elbow on horizontal gas-liquid stratified and annular flow characteristics usin dual wire – mesh sensors, Exp. Ther. Fluid Sci. 59 (2014) 72–87.
[13] G.A. Johansen, P. Jackson, Radioisotope Gauges for Industrial Process Measurements, John Wiley & Sons, Inc., Hoboken,NJ, 2004.
[14] P.A.S. Vasquez, C.H. Mesquita, M.M. Hamada, Methodological analysis of gamma tomography system for large random packed columns, Appl. Radiat. Isot. 68 (2010) 658–661.
[15] C.H. Mesquita, P.A.S. Vasquez, W.A.P. Calvo, D.V.S. Carvalho, L.A. Marcato, J.F.T. Martins, M.M. Hamada, Multi-source third generation computed tomography for industrial multiphase flows applications, in: Proceedings of the IEEE Nuclear Science Symposium Conference Record, New York, 2011, pp. 1294–1302.
[16] C.H. Mesquita, C.C. Dantas, F.E. Costa, D.V.S. Carvalho, T. Madi Filho, P.A.S. Vasquez, M.M. Hamada, Development of a Fourth Generation Industrial Tomography for Multiphase Systems Analysis, in: Proceedings of the IEEE Nuclear Science Symposium Conference Record, New York, 2010, pp. 19–23.
[17] J. Benac, Alternating minimization algorithms for X-ray computed tomography: multigrid acceleration and dual energy application, Tese (Ph.D), Washington University, St. Louis, 2005.
[18] J. Darroch, D. Ratcli, Generalized iterative scaling for log-linear models, Ann. Math. Stat. 43 (1972) 1470–1480.
[19] M. Rabbani, P.W. Jones, Digital Image Compression techniques, Society of Photo-Optical Engineers, Bellingham WA, 1991.
[20] W.T. Eadie, D. Drijard, F.E. James, M. Roos, B. Sadoulet, Statistical Methods in Experimental Physics, North-Holland, Amsterdam (1971), p. 269–271 , ISBN 0-444-10117-9.
[21] The National Institute of Standards and Technology (NIST), The Physical Measurement Laboratory (PML), ⟨http://physics.nist.gov/PhysRefData/Xcom/html/xcom1.html⟩, Visited at August 2015.